

# Quantitative microscope characterization for optical measurements with sub-nm parametric uncertainties

Bryan M. Barnes\*, Jing Qin, Hui Zhou, Richard M. Silver,  
Semiconductor and Dimensional Metrology Division, Physical Measurement Laboratory  
National Institute of Standards and Technology, 100 Bureau Drive MS 8212,  
Gaithersburg, MD 20899-8212

## ABSTRACT

Recently, a new technique called Fourier normalization has enabled the parametric fitting of optical images with multiple or even a continuum of scattered spatial frequencies. Integral to the performance of this methodology is the characterization of the high magnification imaging microscope used in these experiments. Scatterfield microscopy techniques yield the necessary angular resolution required for determining the effects of the illumination and collection paths upon the electric field within the microscope. A multi-step characterization methodology is presented with experimental examples using a microscope operating at  $\lambda = 450$  nm. A prior scatterfield characterization technique for specular reflectors is reviewed and shown to be a special case of the newer generalized approach. Possible implications of this methodology for improved critical dimension measurements are assessed.

**Keywords:** scatterfield microscopy, tool characterization, critical dimension metrology, parametric fitting

## 1. INTRODUCTION

A pressing requirement in optical semiconductor metrology is the measurement of critical dimensions (CDs) within each die that is patterned on a wafer. Currently, CD measurements are performed using scanning electron microscopy (SEM) and optical scatterometers (for optical CD, or OCD). Due to their size, targets for scatterometry are placed outside the dies within the scribe lines that separate these dies from one another. Though these square targets are often less than 40  $\mu\text{m}$  on a side, they are too large to be placed within dies. As dimensions continue to decrease, the ongoing fidelity of OCD measurements at the scribe lines relative to the actual CDs within the dies is threatened. While SEMs are measuring within dies, high-volume manufacturing process control would be aided by access to more measurement locations with higher measurement speeds than can be satisfied by SEM alone. High-throughput, non-destructive in-die measurement capabilities are preferable to adequately ensure the quality of devices in the future.

An optical microscopy method we have developed called scatterfield microscopy can address these issues. Scatterfield microscopes incorporate angle-resolved illumination into a high-magnification imaging platform [1-3]. Like scatterometry, scatterfield microscopy is not inherently limited by resolution limits for arrayed targets, as parametric fitting of simulation-to-experimental results can be performed to determine the underlying geometry of the arrayed features. Angle-resolved scatterfield measurements are enabled by tailoring the Köhler illumination by restricting the light passing through the objective's back focal plane (BFP), shown schematically in Fig. 1, or its conjugate (CBFP). The use of high magnification optics yields focus position as an adjustable parameter for optimizing scatterfield CD measurements and also permits scatterfield target sizes smaller than the field of view that are spatially isolated within the image [4].

Having complex optical trains in the illumination and collection paths, however, necessitates proper characterization of the optical microscope in order to obtain intensities that enable parametric fitting for quantitative scatterfield microscopy. Our previous report [5] on scatterfield microscope characterization outlined methods to convert the measured intensity from certain test samples into a reflectivity using a "tool function" (TF). It was cautioned that these methods were applicable only to test samples that exhibited 0<sup>th</sup> order scattering. In several experiments [6-9], 0<sup>th</sup>-order scattering as functions of incident angle and polarization have been obtained and parametric fits computed using comparisons with a library of simulated values. Using linear regression, intra-library values of the parameters with their parametric uncertainties can be found. Fits have been obtained as the *experimental* data are processed before simulation-to-experiment comparison without arbitrary, tunable parameters.

\*bryan.barnes@nist.gov; phone 1 301 975-3947; fax 1 301 975-4320; <http://www.nist.gov/pml/div683/grp02/om3dnm.cfm>

Extending quantitative parametric fitting capabilities to non-0<sup>th</sup> order targets, ranging from a single isolated line to arrays of three-dimensional transistors in modern semiconductor manufacturing, has required revisiting the microscope characterization, data analysis, and parametric fitting procedures. Recently, we have published our first reports [10,11] of the parametric fitting of an isolated silicon edge with sub-nm parametric uncertainties.

This paper discusses the intricacies in quantitative microscope characterization that were outlined and utilized on optical images with multiple spatial frequencies in Ref. 11. In Section 2, context for this technique is provided by reviewing an earlier scatterfield microscope characterization method [5] and its limitations. The new Fourier normalization methodology is motivated and discussed briefly in Section 3. Specific details and challenges in quantitative microscope characterization are presented in Section 4. For brevity, some vital microscope characterization steps presented in Ref. 5 that are unaltered by the new methodology, such as the determination of the angle of incidence at the sample as a function of CBFP aperture position, are not reviewed in this work.

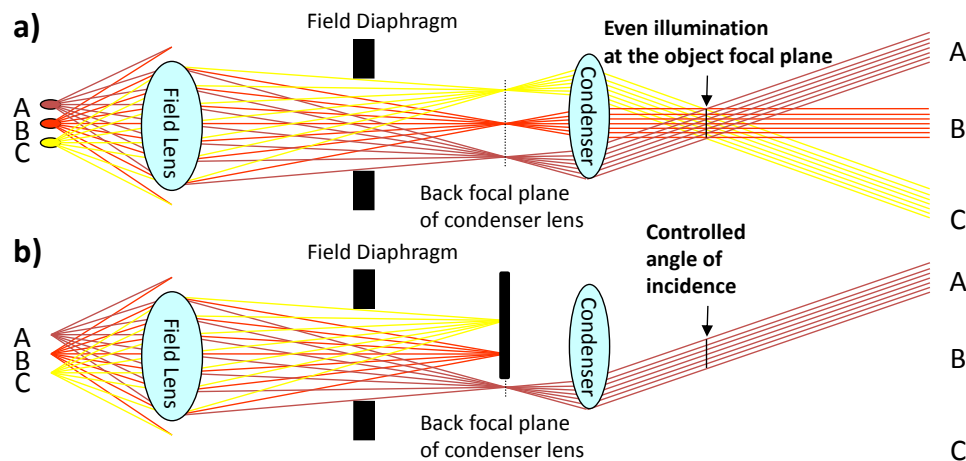


Figure 1. Schematic of the illumination path in a scatterfield microscope. a) Köhler illumination yields spatially uniform light at the sample plane. b) Blocking light at the back focal plane (BFP) of the objective lens produces angularly resolved illumination. By placing an aperture in the BFP (or its conjugate, the CBFP), oblique angles within the objective's numerical aperture (NA) can be produced using these scatterfield techniques.

## 2. MICROSCOPE CHARACTERIZATION FOR 0<sup>TH</sup> ORDER SCATTERING

Before arriving at a more general technique for the parametric fitting of optical images containing a range of spatial frequencies, efforts had been concentrated on processing images with no scattered spatial frequency content coming from the sample. Images with and without spatial content are shown in Fig. 2. The initial microscope characterization techniques presented in Ref. 6 allow an image such as Fig. 2a to be reduced to a scalar reflectivity value. Several angle-resolved scans would be performed to accumulate reflectivity curves for comparison with simulation.

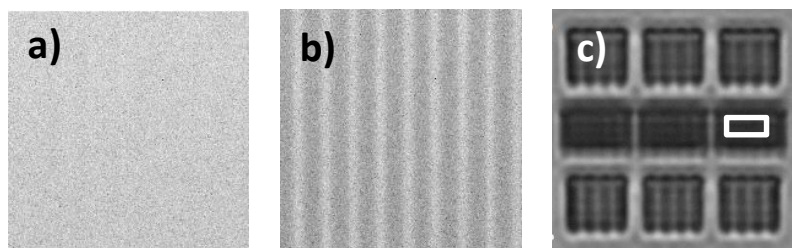


Figure 2. Captured images using visible light for a variety of pitches and array sizes. a) nominally 300 nm pitch,  $\theta_i = 0^\circ$ ,  $\lambda = 450$  nm; b) nominally 600 nm pitch,  $\theta_i = 0^\circ$ ,  $\lambda = 450$  nm; c) line (top, bottom) and trench (middle) arrays smaller than the field-of-view. Finite trench arrays are nominally 434 nm pitch,  $\lambda = 532$  nm  $\theta_i = 0^\circ$ . 0<sup>th</sup> order scattering is observed within the white box but the target as a whole scatters multiple scattering frequencies. Panel c) adapted from Ref. 12.

In Ref. 5 it was shown that the reflectivity of an unknown sample could be determined from knowing the theoretical reflectivity and the reflected intensity from a reference. This was based upon a model of the microscope for which the reflected intensity at the imaging plane was

$$I_{sample}(\theta_i, p) = T_{coll}(\theta_i, p) \times R_{sample}(\theta_i, p) \times T_{illum}(\theta_i, p) \times I_0(\theta_i, p), \quad (1)$$

where  $\theta_i$  is the incident angle,  $I_0$  is the incident intensity,  $T_{illum}$  and  $T_{coll}$  are the transmissivity functions of the illumination and collection paths, respectively, and  $p$  is the polarization. For simplicity,  $\theta$  is used for both polar and azimuthal angles. Though losses in the illumination and collection paths are acknowledged, it was noted that the intensities of two planar reflectors (reflected angle  $\theta_r = -\theta_i$ ) measured under the same experimental conditions could be directly compared as a ratio. A grating acts similarly as a planar reflector if the grating scatters only 0<sup>th</sup>-order light as defined using the grating equation,

$$a(\sin(\theta_i) + \sin(\theta_m)) = m\lambda, \quad (2)$$

where  $a$  is the pitch,  $\lambda$  the wavelength,  $m$  is an integer, and  $\theta_i$  and  $\theta_m$  are the incident angle and  $m^{\text{th}}$  order angle, respectively. If  $a < \lambda/2$ , then no non-zero values of  $m$  are physically realizable from Eqn. 2 for any incident angle. For  $a < \lambda$ , orders may appear depending on the incident angle.

Figure 2b shows a grating with nominally  $a = 600$  nm and  $\lambda = 450$  nm at  $\theta_i = 0^\circ$ . The  $m = \pm 1$  orders are captured within the numerical aperture of the objective lens. Fig. 2c shows a finite array with 0<sup>th</sup>-order scattering in the center of the array. With a high-magnification imaging platform, the scattering in the center can be isolated and processed independently of the higher order content near the edges of the array.

Successful conversion of a 0<sup>th</sup>-order scattering intensity to a reflectivity depends upon compensating for the effects of the transmissivity of the illumination and collection paths. If the reflectivity  $R_{sample}$  of one of two samples is known theoretically and both  $I_{sample}$  are determined, then the reflectivity of the unknown sample can be found. When  $I_{sample,1}$  and  $I_{sample,2}$  are known and divided, the  $T_{illum}$  and  $T_{coll}$  terms in Eqn. 1 cancel out. If  $R_{sample,2}$  is the reference,

$$R_{sample,1}(\theta, p) = I_{sample,1}(\theta, p) \times \frac{R_{sample,2}(\theta, p)}{I_{sample,2}(\theta, p)}. \quad (3)$$

In practice, both the sample and reference intensities contain unwanted additive terms which must be corrected.  $I_{sample}$  differs slightly from the measured intensity due both to glare within the microscope ( $I_{glare}$ ) and the dark current with the charge-coupled device (CCD) camera. Assuming that the dark current is constant among measurements,

$$I_{sample}(\theta, p) = I_{meas}(\theta, p) - I_{glare}(\theta, p). \quad (4)$$

The ratio in Eqn. 3 that converts the reflected intensity into a reflectivity can be described as a tool function for the whole microscope,  $TF_{whole}$ , with

$$TF_{whole}(\theta, p) = \frac{R_{ref}(\theta, p)}{I_{ref}(\theta, p) - I_{glare}(\theta, p)}, \quad (5)$$

and the reflectivity of a flat or zero-order array target determined using

$$R_{target}(\theta, p) = (I_{meas}(\theta, p) - I_{glare}(\theta, p)) \times TF_{whole}(\theta, p). \quad (6)$$

This tool function is the key characterization step needed to enable parametric fitting. The inverse of  $TF_{whole}$  in this derivation is an approximation of the incident intensity,  $I_0(\theta, p)$ .

### 3. FOURIER NORMALIZATION FOR EVALUATING OPTICAL IMAGES

Figure 2b shows a simple example of an image of an array filling the field of view with additional spatial frequency content, thus making it incompatible with the protocol reviewed in Section 2. For an image of  $m = -1, 0, 1$  scattering, the  $T_{coll}$  term from Eqn. 1 would be a function of  $\theta_{m=-1}$ ,  $\theta_{m=0}$  and  $\theta_{m=1}$ , and this  $T_{coll}$  term cannot be divided out for Eqn. 3 above.

Also, applying  $T_{coll}$  to images with multiple orders will not lead to the correct normalization. The intensity that is captured by the camera at the image plane is proportional to the square of the electric field, and the electric field will be

a sum of two or more scattered components for non-0<sup>th</sup> order imaging. The microscope model in Section 2 holds only when the electric field is a single scattered component with no cross terms, and the reflectivity model in Section 2 only holds when that single scattered component is  $m = 0$ . A generalized microscope model requires using the electric field rather than the intensities. The microscope can be expressed as a series of matrix operators acting on an initial electric field  $E_0$  yielding

$$\vec{E}_{image} = \mathbf{C} \cdot \mathbf{S} \cdot \mathbf{I} \cdot \begin{bmatrix} E_{0x} \\ E_{0y} \end{bmatrix}, \quad (7)$$

where the incident electric field is a vector in  $x$  and  $y$ ,  $\mathbf{I}$  represents the operator for the illumination path,  $\mathbf{S}$  represents the scattering for the sample, and  $\mathbf{C}$  is the operator for the collection path. While easily expressed mathematically, the experimental microscope characterization considerations and challenges required to determine  $\mathbf{C}$  and  $\mathbf{I}$  are extensive and nontrivial and are discussed in Section 4.

The enabling technologies behind the normalization of the scattering components in the Fourier plane are the various two- and three-dimensional electromagnetic models used to determine the amplitude and orientation for each scattered component in the electric field. In-house Rigorous Coupled-Wave Analysis (RCWA) [13] and Finite-Difference Time Domain (FDTD) [14] codes have been developed and tested against analytic results and other codes. Both RCWA and FDTD codes yield the full separable, individual scattering orders for both in-plane and conical diffraction. The matrices  $\mathbf{C}$  and  $\mathbf{I}$  are calculated in order to modify the *modeled* scattering matrix  $\mathbf{S}$  to determine the optimal set of parameters that yields the best simulation-to-experiment match. Thus in contrast with the previous approach, parametric fits are now obtained after the *simulated* data are processed before simulation-to-experiment comparison.

#### 4. DETERMINING ILLUMINATION AND COLLECTION TOOL FUNCTIONS

The  $\mathbf{C}$  and  $\mathbf{I}$  matrices are not directly observable, and several steps are required for their calculation. There are two general types of experimental measurements to be performed. First, measurements at the microscope itself yield the condition of the instrument. Second, characterizations of the sensors used to perform the first set of measurements are required to properly treat the data as functions of angle and polarization. Construction of the  $\mathbf{C}$  and  $\mathbf{I}$  matrices for a particular microscope is carried out using this empirical data using a series of matrix equations introduced in Ref. 11. It will be demonstrated that the scatterfield microscope platform enables the angle-resolved quantitative microscope characterization measurements that facilitate the fullest use of the Fourier normalization technique.

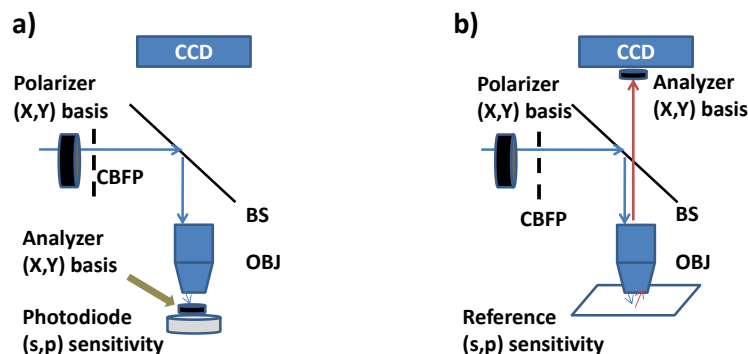


Figure 3. Schematics of measurements at the microscope with beamsplitter BS, objective lens OBJ, and conjugate back focal plane CBFP. a) Illumination path characterization. The analyzer and photodiode are placed directly underneath the objective lens. b) Complete path characterization. The analyzer is placed near the image plane.

At the microscope, the intensities at the sample plane and the imaging plane are most readily accessible. To map the intensities at the sample plane as a function of incident angle, a small aperture is rastered in the conjugate back focal plane (CBFP) of the microscope while a detector, specifically a photodiode, is fixed near the sample plane, shown schematically in Fig. 3a. This rastering yields a map of intensities with respect to aperture CBFP position, permitting later correlation of measured intensities to polar and azimuthal angles of incidence. Four aperture scans are required per iteration for the possible four combinations of a linear polarizer/analyzer pair placed in the illumination path. The polarizer is placed near the CBFP and the analyzer positioned directly between the objective and detector, yielding

intensity maps with respect to  $XX$ ,  $XY$ ,  $YX$ , and  $YY$  polarizations. The  $x$  and  $y$  directions here are determined by the sample plane.

The collection function cannot be accessed directly, thus a measurement through the entire tool path is required using a known reference at the sample plane with the camera as the detector. The measurement of the intensity through the complete optical path as a function of CBFP position and polarization is shown schematically in Fig. 3b. The polarizer is again placed near the CBFP while the analyzer is positioned close to the image plane. Intensity maps with respect to CBFP position are again obtained for the  $XX$ ,  $XY$ ,  $YX$ , and  $YY$  polarization pairs.

Figure 4 shows the raw intensity maps for the dominant polarization pairs ( $XX$ ,  $YY$ ) for the illumination path and the complete path. For both paths,  $XY$  and  $YX$  terms are considered negligible and not included in the equations below. The reference sample in this measurement was an Al mirror. The discrepancy between the illumination path data collected with the photodiode (PD) in Fig. 4a and the complete path data collected with the camera (CCD) in Fig. 4b is due to the photodiode sensitivity depending on both the polarization and the incident angle. Additional sensor characterization is required to use these photodiode data in solving for the matrix  $I$  in Eqn. 7.

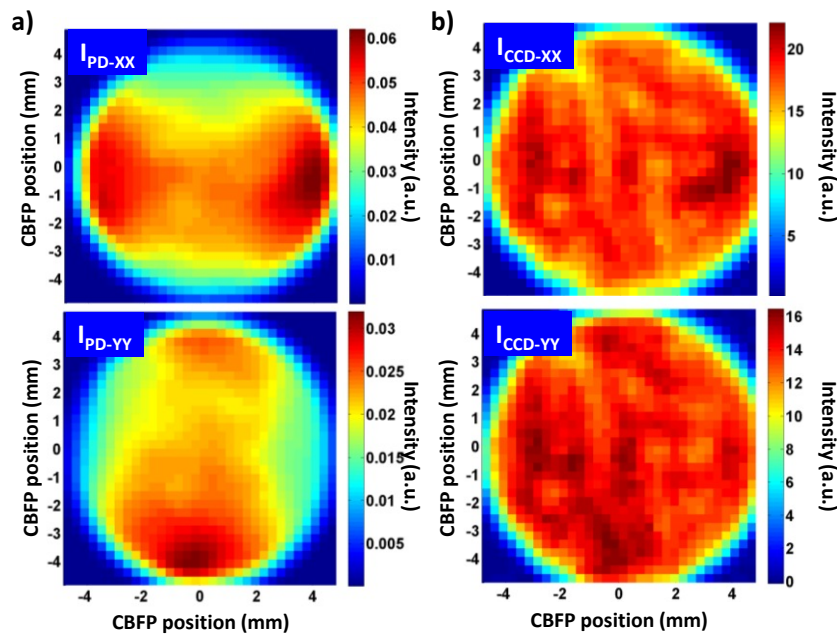


Figure 4. Raw intensity maps measured at the microscope. a) Illumination path intensities registered by a photodiode. b) Complete path intensities registered by a CCD camera. While some polarization effects may be present in the CCD data due to an Al mirror at the sample plane, polarization effects dominate the photodiode data as its sensitivity varies with incident angle and polarization state.

Bench testing of optical components was performed to test the linearity of detectors, the transmittance of polarizer/analyzer pairs in various configurations for oblique angles, and the response of the photodiode as functions of incident angle and polarization state. This latter test is most crucial for converting the data in Fig. 4a into usable data for Fourier normalization.

Figure 5 shows the intensity measured by the photodiode during bench testing at  $\lambda=532$  nm as a function of incident angle for two polarizations. One complication for microscope characterization is that optical components, such as the photodiode, are polarization sensitive in the  $(s,p)$  basis. However, the polarizer/analyzer pairs are fixed in the  $(x,y)$  basis relative to the sample plane and would need to be rotated for all oblique angles to maintain an  $(s,p)$  basis. Ref. 11 outlined the matrix methods required to solve for the  $I$  matrix from Eqn. 7, showing

$$\vec{E}_{PD} = \begin{bmatrix} PD_{ss} & 0 \\ 0 & PD_{pp} \end{bmatrix} \cdot \begin{bmatrix} A_{ss} & A_{ps} \\ A_{sp} & A_{pp} \end{bmatrix} \cdot \begin{bmatrix} I_{xs} & I_{ys} \\ I_{xp} & I_{yp} \end{bmatrix} \cdot \begin{bmatrix} E_x \\ E_y \end{bmatrix}, \quad (8)$$

where  $PD_{ss}$  and  $PD_{pp}$  remove this  $(s,p)$  polarization dependence for the photodiode and  $A$  is an analyzer matrix also characterized at the bench for polarizer/analyzer pairs with respect to  $(s,p)$  polarization. The matrix  $I$  operates on the  $(x,y)$  basis and is operated upon by the  $(s,p)$  basis, which is not only essential for solving Eqn. 8 but also necessary for solving Eqn. 7 as the simulation models utilizes the  $(s,p)$  basis as well for the scattering matrix  $S$ .

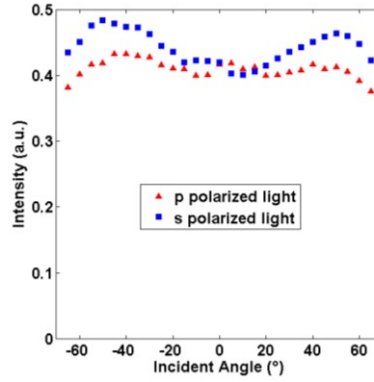


Figure 5. Photodiode characterization for linearly polarized light as a function of incident angle.

In our experiments, illumination is either fully  $x$  polarized or  $y$  polarized at the CBFP, thus with  $\begin{bmatrix} E_x \\ E_y \end{bmatrix}$  either  $\begin{bmatrix} 1 \\ 0 \end{bmatrix}$  or  $\begin{bmatrix} 0 \\ 1 \end{bmatrix}$  and negligible cross-terms  $XY$  and  $YX$  in the illumination path map, the square root of the intensities in Figure 4a are used to estimate  $\vec{E}_{PD}$  with

$$\begin{bmatrix} \sqrt{I_{PD-XX}(\theta, \varphi)} \\ 0 \end{bmatrix} = \begin{bmatrix} PD_{ss} & 0 \\ 0 & PD_{pp} \end{bmatrix} \cdot \begin{bmatrix} A_{ss} & A_{ps} \\ A_{sp} & A_{pp} \end{bmatrix} \cdot \begin{bmatrix} I_{xs} & I_{ys} \\ I_{xp} & I_{yp} \end{bmatrix} \cdot \begin{bmatrix} 1 \\ 0 \end{bmatrix}, \text{ and} \quad (9)$$

$$\begin{bmatrix} 0 \\ \sqrt{I_{PD-YY}(\theta, \varphi)} \end{bmatrix} = \begin{bmatrix} PD_{ss} & 0 \\ 0 & PD_{pp} \end{bmatrix} \cdot \begin{bmatrix} A_{ss} & A_{ps} \\ A_{sp} & A_{pp} \end{bmatrix} \cdot \begin{bmatrix} I_{xs} & I_{ys} \\ I_{xp} & I_{yp} \end{bmatrix} \cdot \begin{bmatrix} 0 \\ 1 \end{bmatrix},$$

allowing the numerical solution for the matrix  $I$ . Once determined, the complete path tool function can likewise be used to solve for the  $C$  matrix using

$$\vec{E}_{CCD} = \begin{bmatrix} A_{xx} & A_{yx} \\ A_{xy} & A_{yy} \end{bmatrix} \cdot \begin{bmatrix} C_{sx} & C_{px} \\ C_{sy} & C_{py} \end{bmatrix} \cdot \begin{bmatrix} S_{ss} & S_{ps} \\ S_{sp} & S_{pp} \end{bmatrix} \cdot \begin{bmatrix} I_{xs} & I_{ys} \\ I_{xp} & I_{yp} \end{bmatrix} \cdot \begin{bmatrix} Ex \\ Ey \end{bmatrix}, \quad (10)$$

and again with negligible cross-terms  $XY$  and  $YX$  in the complete path similar and either  $x$  or  $y$  polarization in the CBFP, we can estimate  $C$  using

$$\begin{bmatrix} \sqrt{I_{CCD-XX}(\theta, \varphi)} \\ 0 \end{bmatrix} = \begin{bmatrix} 1 & 0 \\ 0 & 0 \end{bmatrix} \cdot \begin{bmatrix} C_{sx} & C_{px} \\ C_{sy} & C_{py} \end{bmatrix} \cdot \begin{bmatrix} S_{ss} & S_{ps} \\ S_{sp} & S_{pp} \end{bmatrix} \cdot \begin{bmatrix} I_{xs} & I_{ys} \\ I_{xp} & I_{yp} \end{bmatrix} \cdot \begin{bmatrix} 1 \\ 0 \end{bmatrix}, \text{ and} \quad (11)$$

$$\begin{bmatrix} 0 \\ \sqrt{I_{CCD-YY}(\theta, \varphi)} \end{bmatrix} = \begin{bmatrix} 0 & 0 \\ 0 & 1 \end{bmatrix} \cdot \begin{bmatrix} C_{sx} & C_{px} \\ C_{sy} & C_{py} \end{bmatrix} \cdot \begin{bmatrix} S_{ss} & S_{ps} \\ S_{sp} & S_{pp} \end{bmatrix} \cdot \begin{bmatrix} I_{xs} & I_{ys} \\ I_{xp} & I_{yp} \end{bmatrix} \cdot \begin{bmatrix} 0 \\ 1 \end{bmatrix}.$$

With  $S$  determined through electromagnetic scattering models and matrices  $C$  and  $I$  determined using quantitative microscope characterization, Fourier normalization is facilitated and the parametric fitting of optical images enabled.

## 5. SUMMARY

Quantitative microscope characterization, both at the instrument and at the bench, is essential to achieving simulation-to-experiment fits for optical images with spatial frequency content. The required angle-resolved accuracy is enabled by the scatterfield microscopy platform. Previous intensity-based approaches that permitted rigorous simulation-to-experiment comparisons for 0<sup>th</sup> order scatterers are now encompassed by a generalized model of the microscope that utilizes the electric field. A recently published Fourier normalization technique has demonstrated parametric fits yielding sub-nm parametric uncertainties [11] as the simulated data are processed before simulation-to-experiment comparison without arbitrary, tunable adjustments. Critical dimension measurement capabilities are extended using well characterized high magnification optics with scatterfield microscopy.

## REFERENCES

- [1] R. M. Silver, R. Attota, M. Stocker, M. Bishop, L. Howard, T. Germer, E. Marx, M. Davidson, and R. Larrabee, "High-resolution optical metrology," *Proc. SPIE* **5752**, 67–79 (2005).
- [2] R.M. Silver, B.M. Barnes, R. Attota, J. Jun, M. Stocker, E. Marx, and H. J. Patrick, "Scatterfield microscopy for extending the limits of image-based optical metrology," *Appl. Opt.* **46**, 4248-4257 (2007).
- [3] H.J. Patrick, R. Attota, B. M. Barnes, T. A. Germer, R. G. Dixon, M. T. Stocker, R. M. Silver, M.R. Bishop, "Optical critical dimension measurement of silicon grating targets using back focal plane scatterfield microscopy," *J. Micro. Nano. MEMS MOEMS* **7**, 13012 (2008).
- [4] R. Quintanilha, Y.J. Sohn, B.M. Barnes, and R. Silver, "Sub-50-nm measurements using a 193 nm angle-resolved scatterfield microscope," *Proc. SPIE* 7638, 76381E (2010).
- [5] B. M. Barnes, R. Attota, R. Quintanilha, Y. J. Sohn, and R. M. Silver, "Characterizing a scatterfield optical platform for semiconductor metrology," *Meas. Sci. and Technol.* **22**, 24003 (2011).
- [6] R. M. Silver, B. M. Barnes, A. Heckert, R. Attota, R. Dixon, and J. Jun, "Angle resolved optical metrology", *Proc. SPIE* **6922**, 69221M (2008).
- [7] R. M. Silver, N. F. Zhang, B. M. Barnes, H. Zhou, A. Heckert, R. Dixon, T. A. Germer, and B. Bunday, "Improving optical measurement accuracy using multi-technique nested uncertainties", *Proc. SPIE* 7272, 727202 (2009).
- [8] R. M. Silver, N. F. Zhang, B. M. Barnes, H. Zhou, J. Qin, and R. Dixon, "Nested uncertainties and hybrid metrology to improve measurement accuracy", *Proc. SPIE* **7971**, 797116 (2011).
- [9] N.F. Zhang, R. M. Silver, H. Zhou, and B. M. Barnes, "Improving optical measurement uncertainty with combined multitool metrology using a Bayesian approach," *Appl. Opt.* **51**, 6196-6206 (2012).
- [10] J. Qin, H. Zhou, B. M. Barnes, F. Goasmat, R. G. Dixon, and R. M. Silver, "Multiple-order imaging for optical critical dimension metrology using microscope characterization", *Proc. SPIE* **8466**, 84660G (2012).
- [11] J. Qin, R. M. Silver, B. M. Barnes, H. Zhou, and F. Goasmat, "Fourier domain optical tool normalization for quantitative parametric image reconstruction", *Appl. Opt.* **52**, 6512-6522 (2013).
- [12] B.M. Barnes, R. Attota, L. P. Howard, P. Lipscomb, M.T. Stocker, and R.M. Silver, "Zero-Order and Super-Resolved Imaging of Arrayed Nanoscale Lines using Scatterfield Microscopy, *AIP Conf. Proc.* **931**, 397-401 (2007).
- [13] M. G. Moharam, D. A. Pommet, E. B. Grann, and T. K. Gaylord, "Stable implementation of the rigorous coupled-wave analysis for surface-relief gratings: enhanced transmittance matrix approach," *J. Opt. Soc. Am. A* **12**, 1077–1086 (1995).
- [14] A. Taflov, "Application of the finite-difference time-domain method to sinusoidal steady-state electromagnetic-penetration problems," *IEEE Trans. Electromagn. Compat.* **EMC-22**, 191-202 (1980).